

Compliant joints utilizing the principle of closed form pressure balancing

Sonneveld, D.D.; Nijssen, J.P.A.; van Ostayen, R.A.J.

DOI

[10.1115/1.4062583](https://doi.org/10.1115/1.4062583)

Publication date

2023

Document Version

Final published version

Published in

Journal of Mechanical Design

Citation (APA)

Sonneveld, D. D., Nijssen, J. P. A., & van Ostayen, R. A. J. (2023). Compliant joints utilizing the principle of closed form pressure balancing. *Journal of Mechanical Design*, 145(8), Article 083601.
<https://doi.org/10.1115/1.4062583>

Important note

To cite this publication, please use the final published version (if applicable).
Please check the document version above.

Copyright

Other than for strictly personal use, it is not permitted to download, forward or distribute the text or part of it, without the consent of the author(s) and/or copyright holder(s), unless the work is under an open content license such as Creative Commons.

Takedown policy

Please contact us and provide details if you believe this document breaches copyrights.
We will remove access to the work immediately and investigate your claim.



Dave D. Sonneveld¹

Department of Precision and
Microsystems Engineering,
Delft University of Technology,
Mekelweg 2, Delft 2628 CD, The Netherlands
e-mail: d.d.sonneveld@tudelft.nl

Joep P.A. Nijssen

Department of Precision and
Microsystems Engineering,
Delft University of Technology,
Delft 2628 CD, The Netherlands
e-mail: j.p.a.nijssen@tudelft.nl

Ron A.J. van Ostayen

Department of Precision and
Microsystems Engineering,
Delft University of Technology,
Delft 2628 CD, The Netherlands
e-mail: r.a.j.vanostayen@tudelft.nl

Compliant Joints Utilizing the Principle of Closed Form Pressure Balancing

Compliant joints have significant advantages compared to rigid-body hinges due to a monolithic design and the absence of friction, which prevents effects like wear, backlash, and stick-slip behavior. However, the loading capability is often limited and the support stiffness generally decreases during rotation. A new design principle called closed form pressure balancing has been proposed as a solution to improve these limitations. By using an incompressible fluid as the main compliant element, the support stiffness becomes independent of rotation and buckling no longer limits the loading capability. This work analyzes the fundamental working principle behind closed form pressure balancing and introduces a 2D design model to determine stiffness properties. The design model is validated with a finite element model and used to construct an optimization strategy for optimum joint performance. Additionally, a conversion model and some practical considerations are presented for the transition to a 3D design model. [DOI: 10.1115/1.4062583]

Keywords: compliant joint, universal joint, closed form pressure balancing, large rotation

1 Introduction

Compliant hinges have introduced elastic deformation of flexural elements as an alternative to sliding and rolling contacts in rigid-body hinges. Due to their monolithic design, significant advantages are the absence of wear, backlash, stick-slip behavior, and the need for lubrication, allowing high repeatable motions with high precision [1–3]. General disadvantages include a limited range of motion due to stress concentrations [3] and a moving center of rotation (CoR), called axis drift [4]. Combinations of leaf flexures have been proposed as solutions to these limitations, like the cross-axis flexure [5], cartwheel hinge [3], X2-joint [6], butterfly hinge [7], trapezoidal hinge [8], and CR joints [4]. Other disadvantages, also applicable to these examples, are a limited support stiffness and risk of buckling when the hinges are loaded in compression [9]. Although these effects depend on the design, they often worsen during rotation as leaf flexures lose their support stiffness when deflected [10].

Specific design methods to improve support stiffness and load capability have been proposed. These include the use of inversion and isolation [9], compliant aided rolling contacts [11,12], pre-curved flexures [13], torsional stiffeners [10], and folded leaf springs [14]. However, most methods reintroduce contact surfaces, increase the kinematic complexity, or still suffer from a decreasing performance during rotation. Additionally, as these solutions are based on the use of solid leaf flexures, the design trade-off remains between thinner flexures for a lower rotation stiffness and larger range of motion, and thicker flexures for a higher support stiffness.

This relation between support and rotation stiffness limits the application range of compliant hinges. In positioning mechanisms

for example, the decreasing support stiffness during rotation causes a relatively large footprint compared to the effective workspace [15]. Similarly, biomechanical applications for the replacement of joints loaded in compression, like ankles, hips, or spinal discs, remain difficult to design [16–18]. Other examples that can benefit from axial stiff compliant joints are the connection between a piston and eccentric running track or universal joints in parallel kinematic positioning systems, like large ground based telescopes [19–21]. Improving the support stiffness over a larger rotation could thus increase the range of applications.

Recent work [22] has proposed a new design principle that could improve the support stiffness, utilizing an enclosed incompressible fluid. A prototype has shown an increase in stiffness ratio of the axial support stiffness over the rotation stiffness [22], although the characteristic behavior is still unknown. This current paper presents simplified analytical models to estimate the behavior of this new conceptual principle named closed form pressure balancing. First, the working principle and embodiment are elaborated. An analytical 2D design model to determine characteristic stiffness behavior is presented and verified with a finite element method (FEM) model. The models are then used to analyze the movement of the CoR, study the influence of various design parameters, and develop an optimization method for designing. Finally, 2D to 3D conversion models are introduced that are used to translate the 2D results to a 3D design.

2 Design Model

The design principle analyzed in this work is the use of an incompressible fluid as main compliant element to be loaded under compressive loads [22]. Using a fluid fundamentally changes the working principles behind the axial and rotation stiffnesses. The liquid state allows fluid molecules to freely reorganize and thereby accommodate a change in shape of the volume. Neglecting

¹Corresponding author.

Contributed by the Mechanisms and Robotics Committee of ASME for publication in the JOURNAL OF MECHANICAL DESIGN. Manuscript received July 27, 2022; final manuscript received April 4, 2023; published online June 9, 2023. Assoc. Editor: Girish Krishnan.

inertial and viscous effects, this theoretically results in zero rotation stiffness. However, incompressibility makes the fluid resist any volume changes when loaded in compression, resulting in a significant axial stiffness. The first major advantage compared to flexures is that this working principle of axial stiffness is insensitive to the shape of the fluid volume, theoretically decoupling the axial and rotation stiffnesses. This could prevent a decrease in axial stiffness during rotation and eliminates the trade-off between a high axial stiffness and low rotation stiffness. This characteristic behavior, caused by the closed volume of incompressible fluid, is referred to as “closed form pressure balancing” [22]. However, performance will be influenced by the shape and stiffness of the elastic solid required to contain the fluid. The influence of this elastic body is elaborated on through the use of a simplified 2D analytical model.

2.1 Conceptual Design. A cell is thus needed that optimally transfers the properties of the fluid to a physical joint. In this work, a cell with circular enclosures of thickness t_0 is proposed as shown in Fig. 1. When vertically compressed, fluid is pushed sideways into the enclosure, causing an internal pressure. During rotation and shear, however, no pressure buildup is expected as the volume only needs to change shape, making the rotation and shear stiffnesses fully dependent on the enclosure’s bending stiffness. The circular shape ensures an even distribution of stresses in the material under internal pressure, whereas the curved geometry allows for a low bending stiffness and thus a low rotation stiffness. The rigid connectors are added to clamp the horizontal segments as they potentially provide additional compliance to the enclosures, which would reduce axial stiffness. The second major advantage of this embodiment compared to flexures is that compressive loads are converted to a tensile load in the enclosures, eliminating the risk of buckling. An incidental drawback, however, is a limited shear stiffness due to the low bending stiffness of the enclosure, which is further addressed in Sec. 5.3.

The angle of the circular segment, indicated with θ in Fig. 1, is expected to influence both stiffness and range of motion. For smaller θ the enclosure length increases, which lowers the elongation stiffness and bending stiffness of the enclosures and thus decreases both axial and rotation stiffnesses of the joint. Furthermore, larger arc segments allow larger joint rotations while bending with distributed compliance. As shown in the top right of Fig. 1, smaller arc segments transition to lumped compliance or even require elongation for anti-clockwise rotations of the upper bar to bridge the gap between the endpoints of both connectors, which increases rotation stiffness. Smaller values of θ thus seem favorable, although it reduces axial stiffness. However, as the bending and elongation stiffnesses of the enclosures scale with t_0^3 and t_0^1 respectively, reducing t_0 is considered most efficient to minimize rotation stiffness. Therefore, θ has been increased to $\pi/2$ (rad) to improve axial stiffness while limiting the increase in rotation stiffness due to lumped compliance.

The following sections present two analytical models to predict axial, rotation, and shear stiffnesses. All models assume a linear elastic material and out-of-plane width b of 1 (m). The fluid is assumed incompressible, requiring its initial area A_0 to remain

constant. The horizontal parts of the elastic cell are assumed rigid by clamping of the rigid connectors in Fig. 1.

2.2 Axial Stiffness. The axial compressive stiffness model uses two additional simplifications. First, the enclosures are assumed to maintain a circular shape due to the internal pressure buildup. Second, the enclosure’s bending stiffness is neglected compared to its elongation stiffness for inflation as only thin enclosures are considered to obtain a low rotation stiffness. This includes a free rotation of the enclosures at their connection point to the horizontal segments, as illustrated in Fig. 2.

The modeling approach consists of two parts. The first part is a geometrical description of the required deformation of the inner wall of the enclosure, as schematically shown in the right of Fig. 2. A vertical displacement of the top causes fluid to move into the enclosures. The fluid surface area A_e in a single enclosure for a compression displacement d_h is given by Eq. (1), where L_0 is the length of the horizontal segments and h_0 the initial height of the fluid as in Fig. 1.

$$A_e = (A_0 - L_0(h_0 - d_h))/2 \quad (1)$$

The new geometry of the inner wall follows from two constraints. First, the opening of the inner wall should match with the center volume as given by Eq. (2), where R_a is the radius and θ the opening angle of the inner wall shown in Fig. 2. Second, the volume enclosed by the inner wall should comply with A_e , described in Eq. (3). Together this results in the parameters R_a and θ for every compression d_h , from which the inner wall length c can be obtained using Eq. (4).

$$h_0 - d_h = 2R_a \sin(\theta/2) \quad (2)$$

$$A_e = \pi R_a^2 - 0.5 R_a^2 (\theta - \sin(\theta)) \quad (3)$$

$$c = (2\pi - \theta)R_a \quad (4)$$

The second part of the model uses the derived geometry of the inner wall to determine the axial stiffness of the joint. The steps described in this part are schematically depicted in Fig. 3. Each enclosure is considered as a segment of a hollow cylinder subjected to an internal pressure, for which analytical models exist that describe its linear elastic expansion. As derived by Ref. [23], the radial displacement u of a material point at a center-distance r in a cylinder, subjected to an internal pressure p , is described by Eq. (5), where S_a and S_b are respectively the undeformed inner and outer radii of the cylinder, E the modulus of elasticity, and ν the Poisson’s ratio.

$$u(S_a, S_b, p, r) = \frac{p(1+\nu)}{E(S_b^2 - S_a^2)} \left((1-2\nu)S_a^2 r + \frac{S_a^2 S_b^2}{r} \right) \quad (5)$$

To implement Eq. (5), two additions to the model are required. First, it is noted in the left of Fig. 2 that the endpoints of the enclosure move closer together during compression. To account for this inward movement, the inflation of the enclosures is approached in

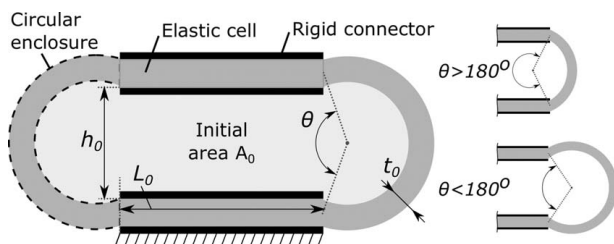


Fig. 1 Embodiment of the pressure balanced compliant joint (left) and the enclosure shape for different angles of θ (right)

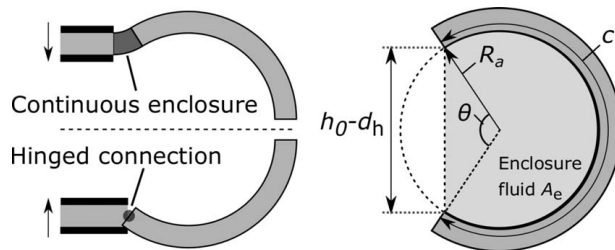


Fig. 2 Enclosure showing the assumption of free rotation (left) and the inner wall geometric description in a deformed configuration for a compression displacement d_h (right)

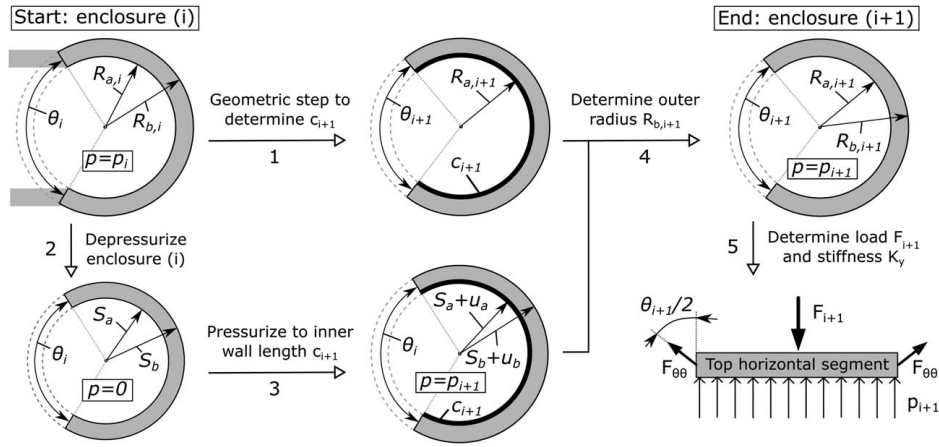


Fig. 3 Flowchart for the calculation of a single inflation step in the enclosure and the corresponding compression force

steps, where in each step Eq. (5) is applied to the updated geometry. The second addition relates to the requirement of Eq. (5) that the initial internal pressure is zero. By using the stepwise approach for inflation, the initial pressure in subsequent modeling steps will be nonzero. Therefore, the geometry at the start of each step is projected back to a state of zero pressure before Eq. (5) is applied. Combined, this results in a sequence of computations for each inflation step. To determine the force F_{i+1} for a compression $d_{h,i+1}$ and the corresponding secant stiffness, this sequence is as follows, as numbered in Fig. 3:

- (1) Using the geometrical analysis, the updated $(i+1)$ inner radius $R_{a,i+1}$, angle θ_{i+1} , and length of the inner wall c_{i+1} are determined based on the compression $d_{h,i+1}$.
- (2) With the pressure p_i and both inner and outer radii $R_{a,i}$ and $R_{b,i}$ known from the previous step (i) , Eq. (5) is applied twice to find the geometry of the enclosure from the previous step, with angle θ_i , for the case its internal pressure would be zero. This results in Eqs. (6) and (7) where both equations are solved simultaneously for S_a and S_b , respectively the inner and outer radii of the enclosure in step (i) under zero internal pressure.

$$R_{a,i} = S_a + u(S_a, S_b, p_i, S_a) \quad (6)$$

$$R_{b,i} = S_b + u(S_a, S_b, p_i, S_b) \quad (7)$$

- (3) For the depressurized enclosure obtained in step 2, the radial displacement u_a required to increase the inner wall length to c_{i+1} is determined using Eq. (8). The pressure p_{i+1} to achieve this displacement u_a from the depressurized state can then be calculated with Eq. (5), using $r = S_a$. Substituting this p_{i+1} again in Eq. (5) using $r = S_b$ yields the displacement u_b of the outer wall.

$$u_a = \frac{c_{i+1}}{2\pi - \theta_i} - S_a \quad (8)$$

- (4) From the displacements u_a and u_b , the enclosure thickness in the updated step $(i+1)$ is determined to find the new outer radius $R_{b,i+1}$ as described in Eq. (9).

$$R_{b,i+1} = R_{a,i+1} + ((S_b + u_b) - (S_a + u_a)) \quad (9)$$

- (5) The pressure p_{i+1} is combined with the elastic force in the enclosures to determine the compression force. As derived by Ref. [23], the tangential stress $\sigma_{\theta\theta}$ as function of position r is described by Eq. (10). Integrating this equation over the wall thickness in depressurized condition, defined by S_a and S_b , results in Eq. (11). Combined with the internal pressure

on the top horizontal segment of the joint, the compression force F_{i+1} is given by Eq. (12), where the elastic force $F_{\theta\theta}$ is added as a tensile force on the top horizontal segment as shown in Fig. 3.

$$\sigma_{\theta\theta} = p \cdot \left(\frac{S_a^2}{S_b^2 - S_a^2} + \frac{S_a^2 S_b^2}{(S_b^2 - S_a^2)r^2} \right) \quad (10)$$

$$F_{\theta\theta,i+1} = p_{i+1} \cdot \left(\frac{b}{S_b^2 - S_a^2} \right) \cdot (S_a S_b^2 - S_a^3) \quad (11)$$

$$F_{i+1} = p_{i+1} \cdot (bL_0) + 2 \cos(\theta_{i+1}/2) \cdot F_{\theta\theta,i+1} \quad (12)$$

The axial secant stiffness K_y then follows from Eq. (13).

$$K_y = \frac{F_{i+1}}{d_{h,i+1}} \quad (13)$$

2.3 Rotation and Shear Stiffnesses. For rotation or horizontal shearing of the upper rigid connector, no significant fluid flow from the center into the enclosures is expected. As this prevents the buildup of pressure, the rotation and shear stiffnesses depend only on the bending stiffness of the enclosures. To analyze this relatively large and non-linear motion, the pseudo-rigid-body (PRB) model in Fig. 4 is constructed, based on a PRB model specific for initially curved beams [24]. Although the basis-PRB model is derived for beams clamped on one side, it is fixed at both ends to the horizontal segments in Fig. 4 by using the symmetry of the enclosure and applying the prescribed angle ζ_1 from Ref. [24] at both ends. With the initial enclosure angle of $\theta = \pi$ (rad), the parameters for the PRB model in Fig. 4 follow directly from Ref. [24] as summarized in Table 1. Note that L_e in Table 1 indicates the initial enclosure length at the middle surface of the wall, opposed to c defined earlier as the enclosure length at the inner wall.

To derive the rotation and shear stiffnesses, the principle of virtual work is applied to the motion of the upper rigid connector and torsion springs between the links. Due to a similarity in derivation, only equations for the right enclosure are shown here. First, the rotation of each spring θ_i in terms of the position $[x_3, y_3]$ and orientation $[\alpha]$ of the upper rigid connector is required. To obtain these rotations, the coordinates $[x_{1RD}, y_{1RD}]$ and $[x_{1RU}, y_{1RU}]$ of the lower and upper springs with stiffness K_1 in Fig. 4 are defined as in Eqs. (14)–(17), where L_0 is the length of the horizontal segments and L_1 and ζ_1 respectively indicate the length and initial angle of the links closest to the rigid connectors.

$$x_{1RD} = \frac{1}{2}L_0 + L_1 \cos(\zeta_1) \quad (14)$$

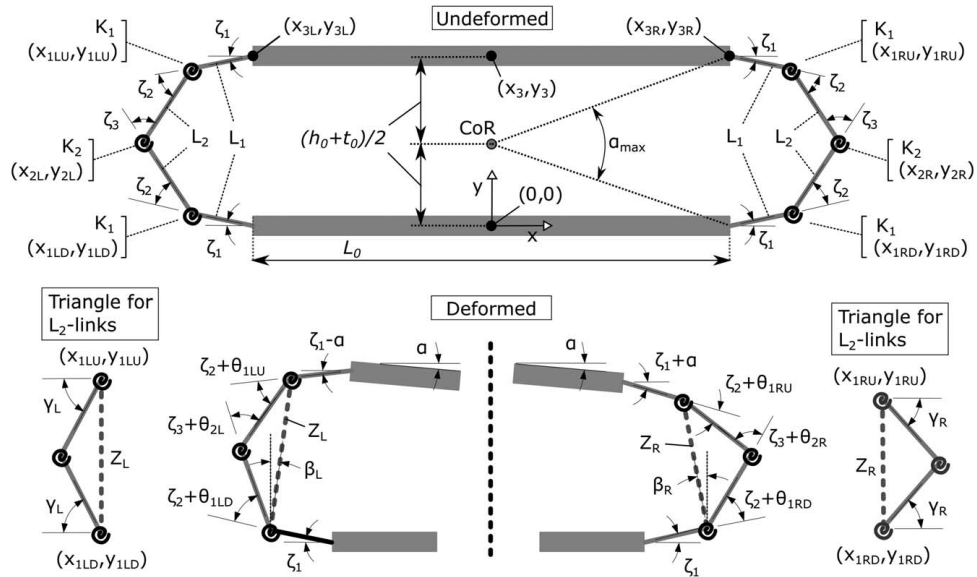


Fig. 4 Model definition of the PRB model used to analyze both the rotation and shear stiffnesses

$$y_{1RD} = L_1 \sin(\zeta_1) \quad (15)$$

$$x_{1RU} = x_3 + \frac{1}{2}L_0 \cos(\alpha) + L_1 \cos(\alpha + \zeta_1) \quad (16)$$

$$y_{1RU} = y_3 - \frac{1}{2}L_0 \sin(\alpha) - L_1 \sin(\alpha + \zeta_1) \quad (17)$$

With above coordinates, the orientations of the middle links of length L_2 can be defined using the triangle in the bottom right of Fig. 4. The distance Z_R between the top and bottom springs is given by Eq. (18). Using this distance Z_R , the triangle orientation β_R and outer angle γ_R follow from Eqs. (19) and (20).

$$Z_R = \sqrt{(x_{1RD} - x_{1RU})^2 + (y_{1RD} - y_{1RU})^2} \quad (18)$$

$$\beta_R = \sin^{-1} \left(\frac{x_{1RD} - x_{1RU}}{Z_R} \right) \quad (19)$$

$$\gamma_R = \sin^{-1} \left(\frac{Z_R}{2L_2} \right) \quad (20)$$

The absolute orientation of the middle links (L_2) can now be described both in terms of the triangle (β_R , γ_R) and the angles between the links (ζ_i , θ_i , α). Combining both options results in the rotation of the springs described by Eqs. (21) and (23).

$$\theta_{1RD} = \gamma_R + \beta_R - \zeta_1 - \zeta_2 \quad (21)$$

$$\theta_{1RU} = \gamma_R - \beta_R - \zeta_1 - \zeta_2 - \alpha \quad (22)$$

$$\theta_{2R} = -\theta_{1RD} - \theta_{1RU} - \alpha \quad (23)$$

Next, static equilibrium is determined by setting the total virtual work W_t for a virtual rotation $\delta\alpha$ to zero as in Eq. (24), where i is the summation over all springs and $\delta\theta_i$ the virtual spring rotation. To evaluate torque T , all $\delta\theta_i$ need to be expressed in terms of $\delta\alpha$. In this model the CoR is assumed in the fluid center, as indicated in Fig. 4 and later verified in the FEM model. Thus, a virtual rotation $\delta\alpha$ also causes virtual displacements δx_3 and δy_3 , leading to Eq. (25) for all $\delta\theta_i$.

$$W_{t, \text{rotation}} = T\delta\alpha - \sum_{i=1}^6 K_i \theta_i \delta\theta_i = 0 \quad (24)$$

$$\delta\theta_i = \left[\frac{\partial\theta_i}{\partial x_3} \left(\frac{h_0 + t_0}{2} \cos \alpha \right) + \frac{\partial\theta_i}{\partial y_3} \left(\frac{h_0 + t_0}{-2} \sin \alpha \right) + \frac{\partial\theta_i}{\partial \alpha} \right] \delta\alpha \quad (25)$$

The secant rotation stiffness K_α is now given by Eq. (26).

$$K_\alpha = \frac{T}{\alpha} = \frac{\left(\sum_{i=1}^6 K_i \theta_i \delta\theta_i \right) / \delta\alpha}{\alpha} \quad (26)$$

For shear stiffness the same derivation is used, where a horizontal force F_x is assumed to translate the upper rigid connector in horizontal direction. This results in Eq. (27) for the virtual work $W_{t, \text{shear}}$ and Eq. (28) for the virtual rotations $\delta\theta_i$.

$$W_{t, \text{shear}} = F_x \delta x_3 - \sum_{i=1}^6 K_i \theta_i \delta\theta_i = 0 \quad (27)$$

$$\delta\theta_i = \frac{\partial\theta_i}{\partial x_3} \delta x_3 \quad (28)$$

The secant shear stiffness K_s is now given by Eq. (29).

$$K_s = \frac{F_x}{x_3} = \frac{\left(\sum_{i=1}^6 K_i \theta_i \delta\theta_i \right) / \delta x_3}{x_3} \quad (29)$$

Table 1 Parameters for the PRB model in Fig. 4

Parameter	Symbol	Value	Unit
Enclosure length	L_e	$\pi(h_0 + t_0)/2$	(m)
Moment of inertia	I	$bt_0^3/12$	(m ⁴)
Length 1	L_1	$0.1296 \cdot L_e$	(m)
Length 2	L_2	$0.3513 \cdot L_e$	(m)
Stiffness 1	K_1	$3.3546 \cdot EI/L_e$	(Nm)
Stiffness 2	K_2	$2.4764 \cdot EI/L_e$	(Nm)
Fixed angle 1	ζ_1	0.2008	(rad)
Initial angle 2	ζ_2	0.7854	(rad)
Initial angle 3	ζ_3	1.1692	(rad)

3 Finite Element Model and Validation

To verify the analytical stiffness models and investigate further performance behavior, the pressure balanced joint is modeled in COMSOL MULTIPHYSICS v5.5. The FEM model consists of a 2D geometry in which the horizontal segments are modeled as rigid domains, following the assumption in the analytical models. The bottom segment is given a fixed constraint while a prescribed displacement/rotation is imposed on the upper segment. The enclosures are modeled as linear elastic material with $E = 1$ (MPa) and $\nu = 0.49$ (–) to simulate an incompressible silicon rubber, also used as reference material throughout the rest of this study. To implement the internal pressure buildup in the incompressible fluid, a pressure p is added as boundary load on the entire inner boundary of the cell. The magnitude of p is defined in a global equation as in Eq. (30), stating p is increased such that the inner area A_{inner} equals the initial area A_0 . A constant 10^5 , the order of number of elements, is added in Eq. (30) to increase the emphasis of this constraint in the overall system of equations and to ensure the constraint to be met when the model converges. The inner area A_{inner} is evaluated using the divergence theorem as described in Eq. (31) [22], where x and y represent the position and n_x and n_y the components of the inwards pointing normal vector \mathbf{n} at the inner boundary.

$$\left(\frac{A_{\text{inner}}}{A_0} - 1 \right) \cdot 10^5 = 0 \quad (30)$$

$$A_{\text{inner}} = - \int_A \frac{n_x \cdot x + n_y \cdot y}{2} dA \quad (31)$$

After imposing a motion, the solid mechanics module determines the resulting deformations in the enclosure using non-linear geometry, a physics controlled “extremely fine” mesh, a relative tolerance of $1 \cdot 10^{-6}$ and the fully coupled MUMPS solver. The resulting stiffness is obtained by evaluating the reaction force from the upper rigid domain.

For pure compression, the upper rigid domain is prescribed a downward translation $u_{0y} = -d_h$, with the horizontal translation (u_{0x}) and rotation (ϕ_0) fixated as no movement is expected in these degrees-of-freedom (DOF). For rotation however, the CoR is unknown. Therefore both translations are not prescribed, allowing the model to translate the upper rigid domain to a state of equilibrium. Similarly for shear, the vertical translation is not prescribed although rotation is again constrained.

3.1 Validation Method. The stiffness from the analytical models is compared to the FEM model for a range of design parameters. Two parameter ratios have been identified that influence the design: (L_0/h_0) and (t_0/h_0) . To independently vary these ratios without scaling the design, a normalized height $h_0 = 1$ (m) is set. Although (L_0/h_0) influences the stiffness, as confirmed in Sec. 4.2, it does not alter the enclosure geometry which affects the validity of the analytical models. Therefore, only (t_0/h_0) ratios are considered here.

To analyze joint configurations able to reach state-of-the-art ranges of motion [14], a maximum ratio of $(L_0/h_0) = 4$ is allowed. This is based on the maximum rotation α_{max} , indicated in Fig. 4 and given by Eq. (32), before internal parts make contact assuming the CoR is in the fluid center.

$$\alpha_{\text{max}} = 2 \tan^{-1}(h_0/L_0) \quad (32)$$

Therefore, a range of [2; 4] for (L_0/h_0) is analyzed in this work, of which $(L_0/h_0) = 3$ is used for validation. The (t_0/h_0) ratio is chosen as [0.01; 0.10] to account for thicknesses from a general plate ratio up to one order thicker enclosures. For the axial stiffness, the compression is approached in $n = 25$ steps with a maximum compression ratio $C_{\text{ratio}} = 5\%$, defined in Eq. (33). This C_{ratio} is chosen such that the strain of the enclosure remains below 10% as a linear elastic material model is used [25]. Due to geometrical

limitations of the PRB model, the rotation and shear stiffnesses are evaluated from the neutral position up to 5 deg rotation and a translation dx with shear ratio $S_{\text{ratio}} = 20\%$ as in Eq. (34).

$$C_{\text{ratio}} = \frac{d_h}{h_0} = 0.05 \quad (33)$$

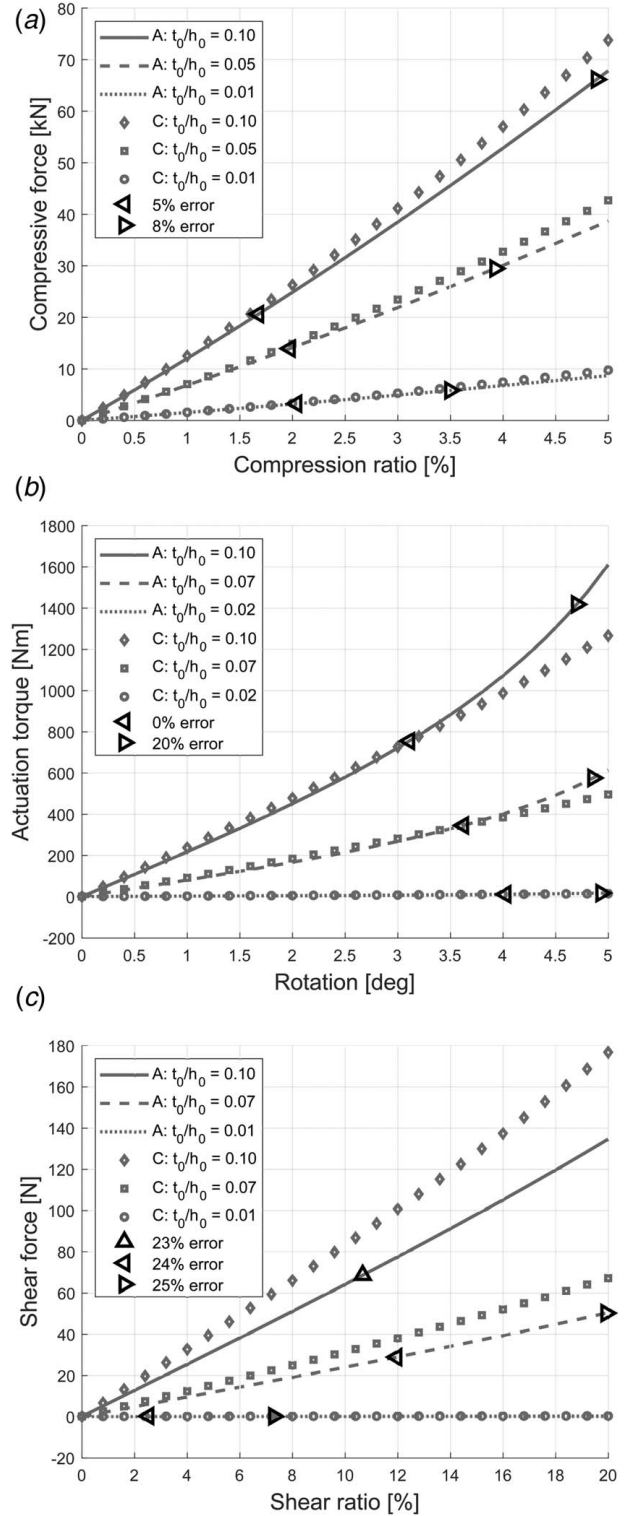


Fig. 5 Comparison between the analytical models (A) and the COMSOL model (C) for the (a) axial, (b) rotation, and (c) shear stiffnesses, using $E = 1$ (MPa), $\nu = 0.49$ (–), and $h_0 = 1$ (m). The error markers indicate the error of the analytical model relative to COMSOL.

$$S_{\text{ratio}} = \frac{d_x}{h_0} = 0.20 \quad (34)$$

Figure 5 presents the comparison between the analytical and FEM model. Different combinations of (t_0/h_0) ratios are plotted to optimally present the encountered effects.

4 Joint Behavior and Implementation

Both analytical and FEM models are used in this section to analyze the CoR and characteristic stiffness behavior and to introduce an optimization strategy. Additionally, a conversion model and some practical considerations are presented for 3D design implementations.

4.1 Center of Rotation. Several methods to determine the CoR exist in literature [8,26]. Constructing the instantaneous center is considered most accurate and implemented as described in Ref. [26]. First, the displacements of the endpoints of the upper rigid connector are tracked in the FEM model during rotation. For each displacement, a perpendicular bisector is constructed. The intersection of the two bisectors then indicates the CoR.

From simulations with varying parameters, only the (L_0/h_0) ratio showed to significantly influence the axis drift. This is expected as the position of the upper rigid connector depends on the constant volume constraint and only the (L_0/h_0) ratio influences the volume shape and magnitude. For all parameters, the instantaneous

CoR is initially located in the fluid center, as indicated in Fig. 4. When normalized to the length L_0 , the drift of the CoR during rotation for various (L_0/h_0) ratios is relatively constant as shown in Fig. 6(a), showing a predominant translation to the right. To interpret the effect of this axis drift, the normalized displacement of the upper rigid connector is shown in Fig. 6(b), evaluated at its midpoint (x_3, y_3) . As the CoR appears to translate faster to the right, the rigid connector moves slightly upwards.

4.2 Parametric Analysis and Optimization. Using the analytical models, the influence of the design parameters on stiffness behavior is analyzed for $h_0 = 1$ (m). Only the axial and rotation stiffnesses are considered here as the shear stiffness is inherently low. However, if shear deformations cannot be allowed in an intended application, measures are needed as will be suggested in Sec. 5. The analysis uses a compression of $C_{\text{ratio}} = 1\%$, well within the linear range of the deformation curve of Fig. 5(a). For rotation stiffness, the analytical model was shown to be most accurate at 3.5 deg rotation for $(L_0/h_0) = 3$. However, the vertical compression of the circular enclosure scales linearly with L_0 for a constant rotation. Therefore, the optimum rotation α_{opt} to determine rotation stiffness with a minimal error at other (L_0/h_0) ratios is corrected by Eq. (35) in this analysis.

$$\alpha_{\text{opt}} = 3.5 \text{ deg} \cdot \frac{3}{(L_0/h_0)} \quad (35)$$

The result of the stiffness analysis is shown in Fig. 7. The effect of the (t_0/h_0) ratio on both stiffnesses corresponds with the assumption in Sec. 2.1 that thickness t_0 scales the axial and rotation stiffnesses with t_0^1 and t_0^3 respectively. Looking at the (L_0/h_0) ratio, both stiffnesses scale quadratic which is explained as follows. For a given compression d_h , the fluid is pushed sideways into the enclosures, and with it the pressure that is generated, increases with L_0^1 . As this pressure acts on the upper surface also increased by L_0^1 , the axial stiffness scales with $(L_0/h_0)^2$. For a given rotation, the vertical displacements of the circular enclosures, and with their reaction forces, increase with L_0^1 . With the moment-arms of these reaction forces also related to L_0^1 , the rotation stiffness scales with $(L_0/h_0)^2$ as well.

Additionally, the stiffness ratio K_{ratio} given in Eq. (36) is analyzed as suggested by Ref. [4]. This non-dimensionless ratio indicates the joints performance as an axial stiff rotational joint because the unconstrained rotational DOF should have a relatively low stiffness compared to the constrained axial DOF [8]. The result of this analysis is shown in Fig. 8(a). The (L_0/h_0) ratio has no influence on K_{ratio} as both axial and rotation stiffnesses scale with $(L_0/h_0)^2$. Although decreasing thickness t_0 significantly improves the stiffness ratio, it must be noted that it decreases the axial stiffness as well.

$$K_{\text{ratio}} = \frac{K_y}{K_x} \quad (36)$$

To decide on the trade-off in thickness t_0 , an optimization is proposed with an example shown in Fig. 8(b). The objective is to maximize K_{ratio} for optimum performance as axial stiff rotational joint. A minimum axial stiffness (e.g., $K_y > 5 \cdot 10^5$ (N/m)) should be defined as constraint for the application. Additionally, Eq. (32) can be used to constrain the maximum (L_0/h_0) ratio for a desired range of motion (e.g., $\alpha_{\text{max}} > 30$ deg). As the objective increases for smaller (t_0/h_0) ratios, the optimum parameters are then located at the intersection of both constraints, as indicated in Fig. 8(b).

4.3 2D to 3D Design Conversion. So far a 2D embodiment has been analyzed for the characteristics of closed form pressure balancing, but extruding the 2D geometry does not result in a feasible design as fluid will leak from the front and back. Potential 3D embodiments are proposed in Fig. 9, including a rectangular

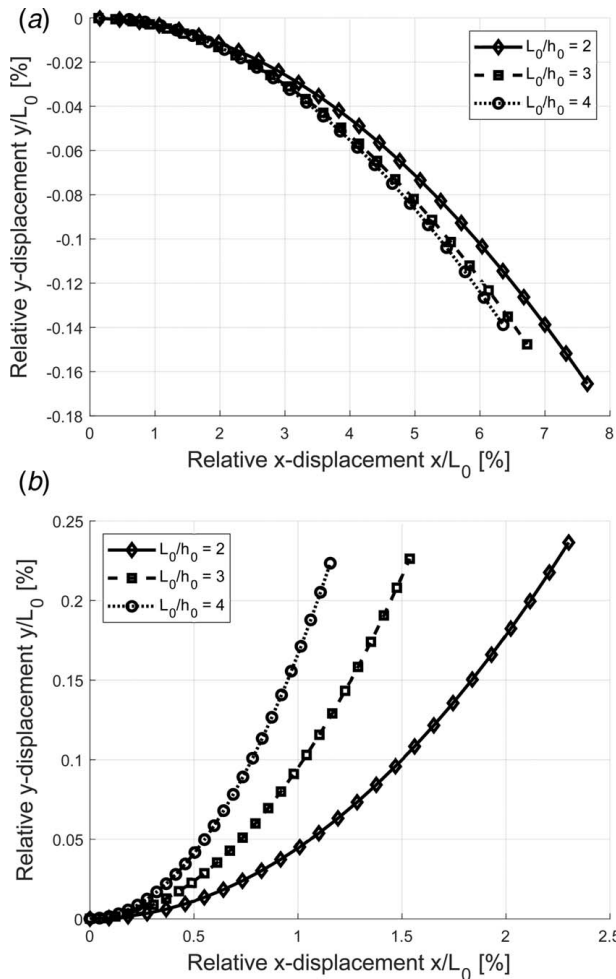


Fig. 6 Normalized displacement of (a) the CoR and (b) the upper midpoint (x_3, y_3) during a 5 deg clockwise rotation, simulated for $(t_0/h_0) = 0.05$, $h_0 = 1$ (m), $E = 1$ (MPa), and $\nu = 0.49$ (—)

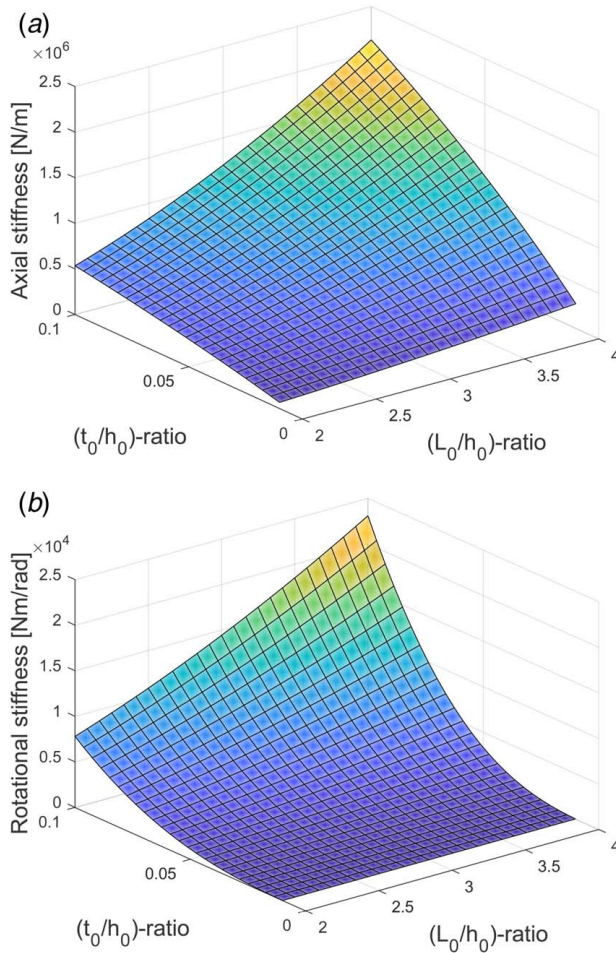


Fig. 7 Parametric analysis on the (a) axial and (b) rotation stiffnesses for $h_0 = 1$ (m), $E = 1$ (MPa) and $\nu = 0.49$ (—)

design for a single-DOF hinge and a circular design for a double-DOF universal joint, using an axisymmetric topology. The double curvature of the enclosures in Fig. 9 indicates that a significant shearing motion is geometrically limited. Therefore, only designs with rotational DOF are considered useful.

This step to 3D designs does influence the stiffness properties. The rotation stiffness increases due to the double curvature of the enclosure and stiffness from the front and back segments. As the double curvature depends on the 3D shape, a general correction factor for this increase is not considered possible. The axial stiffness on the other hand decreases as the fluid also moves into the added enclosure segments during compression, reducing the overall required inflation. This effect can be generally predicted as the enclosure inflation in 3D is similar to 2D, apart from a circumferential component that will be discussed in Sec. 5. The prediction uses the increase in enclosure length from the 2D to 3D embodiment, defined as the circumference of the rigid connector adjacent to an enclosure as indicated in Fig. 9. With all enclosure segments in parallel, the axial stiffness is expected to scale inversely proportional to this enclosure length. As will be shown with an example for both the rectangular and circular designs, two steps define the stiffness prediction:

- (1) The out-of-plane width b in the 2D analytical model is scaled to equalize the top surface areas of the 2D and 3D design for an equal volume displacement during compression. For the examples, this results in Eqs. (37) and (38), where w is the width of the rectangular joint as in Fig. 9.

$$b_{\text{rectangular}} = w \quad (37)$$

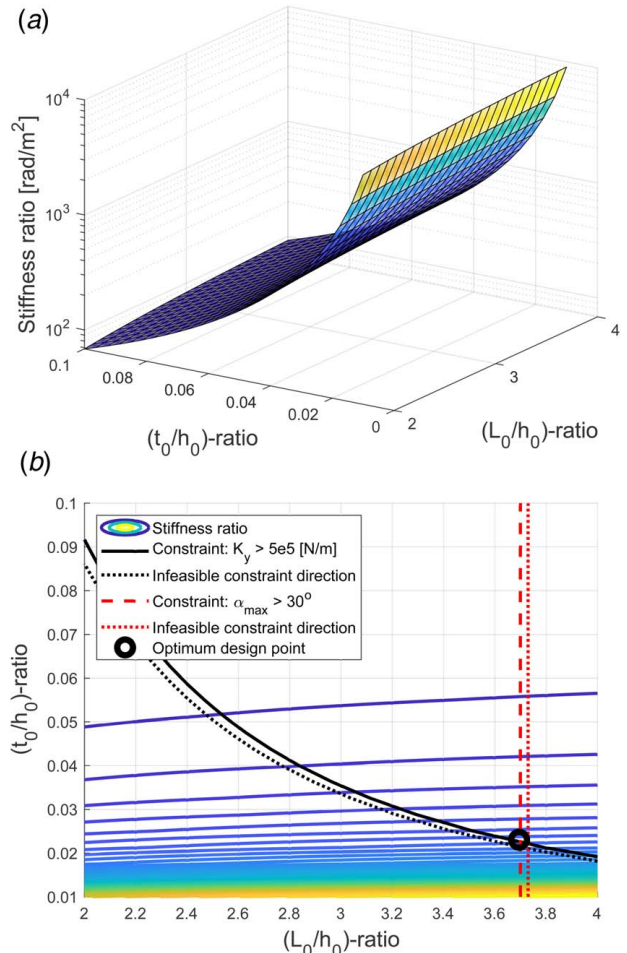


Fig. 8 (a) Analysis of the stiffness ratio for $h_0 = 1$ (m), $E = 1$ (MPa), $\nu = 0.49$ (—) and (b) an example of an optimization strategy

$$b_{\text{circular}} = \pi L_0 / 4 \quad (38)$$

- (2) A correction factor f_{cor} is defined to predict the 3D axial stiffness from the 2D result as in Eq. (39). The factor is based on the ratio of the 2D (L_{2D}) and 3D (L_{3D}) enclosure lengths, where L_{2D} only consists of two segments at the sides. For the examples, this results in Eqs. (40) and (41).

$$K_{y,3D} = f_{\text{cor}} \cdot K_{y,2D} \quad (39)$$

$$f_{\text{cor,rectangular}} = \frac{L_{2D}}{L_{3D}} = \frac{2b_{\text{rectangular}}}{2(w + L_0)} \quad (40)$$

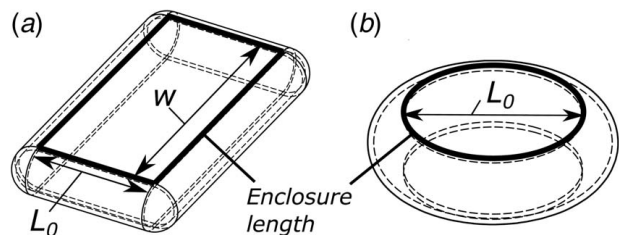


Fig. 9 3D embodiments of the pressure balanced joint as (a) a single-DOF rotational joint and (b) double-DOF universal joint

Table 2 Comparison between the predicted and simulated 3D axial stiffness of a rectangular and circular 3D designs

Joint type	Predicted K_y	Simulated K_y
Rectangular	$2.73 \cdot 10^6$ (N/m)	$2.74 \cdot 10^6$ (N/m)
Circular	$8.02 \cdot 10^5$ (N/m)	$8.61 \cdot 10^5$ (N/m)

$$f_{\text{cor,circular}} = \frac{L_{2D}}{L_{3D}} = \frac{2b_{\text{circular}}}{\pi L_0} = \frac{1}{2} \quad (41)$$

To validate the prediction, both designs were implemented in a 3D COMSOL model using the approach described in Sec. 3. Different however is the use of a 3D geometry, to model both radial and circumferential expansions, and the 3D volume integral from Eq. (42), to evaluate the inner volume V_{inner} for incompressibility. Simultaneously, the axial stiffnesses were predicted with the analytical steps presented above. The parameters used are $h_0 = 1$ (m), $(L_0/h_0) = 3$, $(t_0/h_0) = 0.05$, and width $w = 6$ (m). The results, evaluated at a compression ratio $C_{\text{ratio}} = 1\%$, are given in Table 2.

$$V_{\text{inner}} = - \int_A \frac{n_x \cdot x + n_y \cdot y + n_z \cdot z}{3} dA \quad (42)$$

4.4 Combined Loadcases. The axial and rotation stiffnesses were separately analyzed in preceding sections for the characteristics of closed form pressure balancing. However, a more realistic load case will be one with an axial load during rotation, causing an internal pressure that pushes the enclosures into a circular shape. As this negatively influences their bending stiffness, an increase in rotation stiffness is expected for increasing axial loads. It is therefore important to identify its effect on performance.

Two simulations are compared for a rotation of the 3D circular design with its parameters from Sec. 4.3. First, the upper rigid domain is rotated over 10 deg while it is free to translate vertically. Second, a constant vertical load F_{load} on the upper domain is simulated during rotation by prescribing a variable translation dz to it. This dz is defined in a global equation stating that its value is increased such that the vertical reaction force F_z equals F_{load} as in Eq. (43). For two axial loads, corresponding to a compression ratio of 1% and 2%, the resulting actuation torque is shown in Fig. 10.

$$\left(\frac{F_z}{F_{\text{load}}} - 1 \right) = 0 \quad (43)$$

5 Discussion

5.1 Design Model. The analytical design model presented in Sec. 2, able to estimate the onset axial and rotation stiffnesses within 10% error, provides a design tool to obtain initial design parameters for further optimization. However, three limitations exist. Application of the model is restricted to relative small compressions, because of the use of a linear elastic material, and to limited rotations, as the two middle links in the PRB model align at some point. Furthermore, the constraint of a constant inner volume cannot be implemented in the PRB model and only embodiments with specific angular segments θ can be analyzed for which parameters of the PRB model exist [24]. These last two are limitations as they prevent an analytical analysis of combined loadcases during rotation.

5.2 Finite Element Method Model and Validation. Section 3 introduced a FEM modeling approach and validation of the analytical models, requiring two remarks. First, the use of Young's modulus $E = 1$ (MPa) is not considered to influence the validation or performances presented, apart from stiffness magnitudes, as all

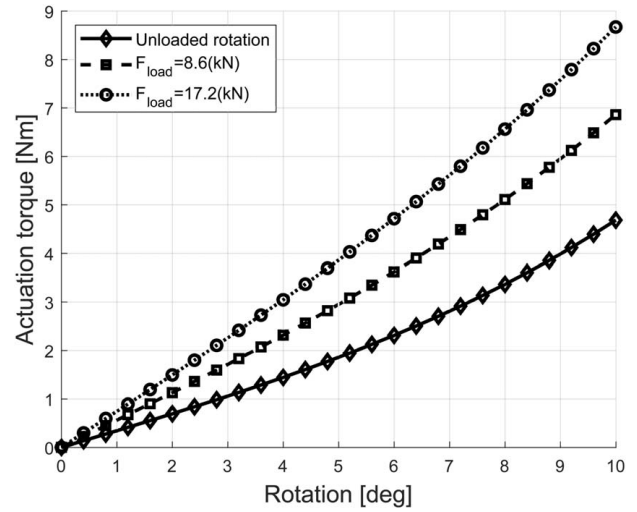


Fig. 10 Effect of a combined loadcase with an axial load on the rotation stiffness in a 3D circular design, simulated for $(L_0/h_0) = 3$, $(t_0/h_0) = 0.05$, $h_0 = 1$ (m), $E = 1$ (MPa), and $\nu = 0.49$ (—)

stiffnesses scale linearly with E . Second, although no experimental validation has been presented in this paper, it is noted that a prototype has been tested in a case study in Ref. [27]. Also, a similar FEM modeling approach was experimentally validated in Ref. [22].

The remainder of this section discusses the validation results from Fig. 5. For the axial stiffness, a structural underestimation of the simulated stiffness is seen. This can be explained by neglecting the bending stiffness in both the enclosures and their connection points to the rigid connectors in the analytical model. At relative small compressions, this effect is more significant for thicker enclosures, as expected. However, at larger compressions the analytical model performs better for thicker enclosures. This is probably caused by a growing error in the adapted enclosure thickness (step 4 in Fig. 3), which is more significant for thin enclosures.

The analytical rotation stiffness shows an initial underestimation before rapidly increasing, which is explained by the PRB model. Links L_1 next to the horizontal segments are fixed at an angle ζ_1 , so the required deformation is distributed over all torsion springs. In the FEM model however, the enclosures maintain more circular for a constant inner volume, resulting in larger enclosure deformations close to the rigid connectors and increased stiffness. At larger joint rotations, the PRB model approaches the singularity where the middle links align. As this requires large rotations in the torsion springs, the rotation stiffness rapidly increases.

The analytical shear stiffness shows a structural underestimation as well. Similar to the rotation stiffness, the constraint on incompressibility causes larger deformations close to the rigid connectors in the FEM model, resulting in a larger stiffness. Despite that, it is noted that the shear stiffness is significantly lower than the axial stiffness. This can be explained by the rolling motion of the enclosures during a horizontal movement of the upper rigid connector, best compared to the motion seen in tape loops [28].

5.3 Joint Performance. The assumption on the central position of the CoR was verified in Sec. 4.1, although Fig. 6 showed that the CoR moves sideways during rotation. This axis drift, relative to the joints dimensions, is significant compared to most conventional compliant joints [29]. Additionally, the axis drift is expected to increase significantly for combined load cases as the compressive load creates a horizontal force component during rotation. Due to the relative low shear stiffness, this horizontal force can translate the upper part of the joint sideways and obstruct the joint's functionality as a hinge. Adding stiffness elements to improve the shear stiffness is therefore recommended, as demonstrated in the

case study in Ref. [27]. Here, an intersecting set of wires was added inside the cell between the top and bottom rigid connectors that created shear stiffness without affecting the rotation stiffness.

The performance in terms of stiffnesses was presented in Sec. 4.2. For this analysis, only secant stiffnesses have been used as Fig. 5 showed all stiffnesses to behave approximately linear. With respect to the stiffness ratio and optimization, two remarks are made. First, the stiffness ratio is not dimensionless and improves for smaller designs. Second however, stresses and failure have not been considered. When included, they will limit the minimum size and achievable stiffness ratio as stresses increase for smaller designs. Also with respect to the range of motion, it is recommended to analyze material behavior in future research.

5.4 Conversion to 3D Designs. Section 4.3 described the negative effect of conversion to 3D designs on the axial and rotation stiffnesses and showed in Table 2 that the 3D axial stiffness can be estimated from the 2D model. The underestimation for the circular embodiment in Table 2 is the result of this particular 3D shape, that apart from the radial expansion as in the 2D design also expands in circumferential direction, which is not included in the prediction method. In the rectangular shape, this is less relevant as most segments only expand radially. Although no 3D prediction is presented for the rotation stiffness, it is noted that this stiffness is not required in the optimization for finding initial design parameters, as described in Sec. 4.2.

Another aspect for 3D implementations however, is the effect of combined load cases as presented in Sec. 4.4. Figure 10 confirms that compressive loads during a rotation significantly increase rotation stiffness. An additional explanation for this effect is a difference in deformation of the enclosure at opposite sides of the joint. On one side the rigid connector tips move apart resulting in an inward movement of the enclosure, while on the other side the tips move closer together resulting in an outward movement of the enclosure. With the pressure in both enclosures being equal, the shape difference causes a reaction torque on the upper rigid domain, increasing rotation stiffness. As this effect is inherent to the enclosures, it should be taken into account when designing for a maximum rotation stiffness.

6 Conclusion

This work presents the characteristics of closed form pressure balancing, a design approach to improve axial performance in compliant rotational joints. By using an incompressible fluid, the axial and rotational stiffnesses become decoupled which prevents an axial stiffness decrease during rotation. Additionally, compressive forces are converted to tensile loads which prevent buckling and thus increase loading capability. Analytical and FEM models developed are capable to determine initial stiffnesses of a 2D embodiment and provide a design tool to find optimum design parameters. With the proposed design, relative large ranges of motion can be achieved that only depend on joint length. Optimal joint performance in terms of stiffnesses is achieved at smaller enclosure thicknesses, although a minimum axial stiffness should be maintained. The center of rotation, initially at the center of the joint, shows a horizontal drift up to 8% relative to the joints length during rotation. However, a relative low shear stiffness makes the CoR susceptible to external loads, for which additional elements in parallel are recommended. Additionally, a conversion model is presented capable to predict the axial stiffness in 3D designs from the 2D model. Finally, axial loads are shown to significantly increase the rotation stiffness, which needs to be taken into account in the design process.

Conflict of Interest

There are no conflicts of interest.

Data Availability Statement

The datasets generated and supporting the findings of this article are obtainable from the corresponding author upon reasonable request.

References

- [1] Howell, L. L., 2013, *21st Century Kinematics*, Springer, London, pp. 189–216.
- [2] Lusty, C., Bailey, N. Y., and Keogh, P. S., 2017, “A Comparison of the Capacity for Precise Motion Control Between Hinged Joints and Flexure Joints,” *Proceedings of the ASME 2017 International Mechanical Engineering Congress and Exposition. Volume 4A: Dynamics, Vibration, and Control*, Tampa, FL, Nov. 3–9, ASME, p. V04AT05A019.
- [3] Kang, D., and Gweon, D., 2013, “Analysis and Design of a Cartwheel-Type Flexure Hinge,” *Precis. Eng.*, **37**(1), pp. 33–43.
- [4] Trease, B. P., Moon, Y. -M., and Kota, S., 2004, “Design of Large-Displacement Compliant Joints,” *ASME J. Mech. Des.*, **127**(4), pp. 788–798.
- [5] Jensen, B. D., and Howell, L. L., 2002, “The Modeling of Cross-Axis Flexural Pivots,” *Mech. Mach. Theory*, **37**(5), pp. 461–476.
- [6] Martin, J., and Robert, M., 2011, “Novel Flexible Pivot With Large Angular Range and Small Center Shift to be Integrated into a Bio-Inspired Robotic Hand,” *J. Intel. Mater. Syst. Struct.*, **22**(13), pp. 1431–1437.
- [7] Henein, S., Spanoudakis, P., Droz, S., Myklebust, L. I., and Onillon, E., 2003, “Flexure Pivot for Aerospace Mechanisms,” 10th European Space Mechanisms and Tribology Symposium, San Sebastian, Spain, Sept. 24–26, pp. 285–288.
- [8] Xu, P., Jingjun, Y., Guanghua, Z., Shusheng, B., and Zhiwei, Y., 2008, “Analysis of Rotational Precision for an Isosceles-Trapezoidal Flexural Pivot,” *ASME J. Mech. Des.*, **130**(5), p. 052302.
- [9] Guérinot, A. E., Magleby, S. P., Howell, L. L., and Todd, R. H., 2004, “Compliant Joint Design Principles for High Compressive Load Situations,” *ASME J. Mech. Des.*, **127**(4), pp. 774–781.
- [10] Wiersma, D. H., Boer, S. E., Aarts, R. G. K. M., and Brouwer, D. M., 2014, “Design and Performance Optimization of Large Stroke Spatial Flexures,” *ASME J. Comput. Nonlinear. Dyn.*, **9**(1), p. 011016.
- [11] Cannon, J. R., Lusk, C. P., and Howell, L. L., 2005, “Compliant Rolling-Contact Element Mechanisms,” *Proceedings of the ASME 2005 International Design Engineering Technical Conferences and Computers and Information in Engineering Conference. Volume 7: 29th Mechanisms and Robotics Conference, Parts A and B*, Long Beach, CA, Sept. 24–28, American Society of Mechanical Engineers Digital Collection, pp. 3–13.
- [12] Jeanneau, A., Herder, J., Laliberté, T., and Gosselin, C., 2004, “A Compliant Rolling Contact Joint and Its Application in a 3-DOF Planar Parallel Mechanism With Kinematic Analysis,” *Proceedings of the ASME 2004 International Design Engineering Technical Conferences and Computers and Information in Engineering Conference. Volume 2: 28th Biennial Mechanisms and Robotics Conference, Parts A and B*, Salt Lake City, UT, Sept. 28–Oct. 2, American Society of Mechanical Engineers Digital Collection, pp. 689–698.
- [13] Brouwer, D. M., Meijaard, J. P., and Jonker, J. B., 2009, “Elastic Element Showing Low Stiffness Loss at Large Deflection,” *Proceedings of the 24th Annual Meeting of the American Society of Precision Engineering*, Monterey, CA, pp. 30–33.
- [14] Naves, M., Aarts, R. G. K. M., and Brouwer, D. M., 2019, “Large Stroke High Off-Axis Stiffness Three Degree of Freedom Spherical Flexure Joint,” *Precis. Eng.*, **56**, pp. 422–431.
- [15] Folkersma, K. G. P., Boer, S. E., Brouwer, D. M., Herder, J. L., and Soemers, H. M. J. R., 2012, “A 2-DOF Large Stroke Flexure Based Positioning Mechanism,” *Proceedings of the ASME 2012 International Design Engineering Technical Conferences and Computers and Information in Engineering Conference. Volume 4: 36th Mechanisms and Robotics Conference, Parts A and B*, Chicago, IL, Aug. 12–15, American Society of Mechanical Engineers Digital Collection, pp. 221–228.
- [16] Nguyen, T. T., Dao, T. -P., and Huang, S. -C., 2017, “Biomechanical Design of a Novel Six DOF Compliant Prosthetic Ankle-Foot 2.0 for Rehabilitation of Amputee,” *Proceedings of the ASME 2017 International Design Engineering Technical Conferences and Computers and Information in Engineering Conference. Volume 5A: 41st Mechanisms and Robotics Conference*, Cleveland, OH, Aug. 6–9, American Society of Mechanical Engineers Digital Collection, p. V05AT08A013.
- [17] Nguyen, T. T., Le, H. G., Dao, T. -P., and Huang, S. -C., 2017, “Evaluation of Structural Behaviour of a Novel Compliant Prosthetic Ankle-Foot,” *2017 International Conference on Mechanical, System and Control Engineering (ICMSC)*, St. Petersburg, Russia, pp. 58–62.
- [18] Halverson, P. A., Howell, L. L., and Bowden, A. E., 2009, “A Flexure-Based Bi-Axial Contact-Aided Compliant Mechanism for Spinal Arthroplasty,” *Proceedings of the ASME 2008 International Design Engineering Technical Conferences and Computers and Information in Engineering Conference. Volume 2: 32nd Mechanisms and Robotics Conference, Parts A and B*, Brooklyn, NY, Aug. 3–6, American Society of Mechanical Engineers Digital Collection, pp. 405–416.
- [19] Nijssen, J., Kempenaar, A., and Diepeveen, N., 2018, “Development of an Interface Between a Plunger and an Eccentric Running Track for a Low-Speed

- Seawater Pump,” Fluid Power Networks: Proceedings 11th International Fluid Power Conference, Aachen, Germany, Mar. 19–21, pp. 370–379.
- [20] Sneed, R. C., Cash, M. F., Chambers, T. S., and Janzen, P. C., 2010, “Six Degrees of Freedom, Sub-Micrometer Positioning System for Secondary Mirrors,” *Proc. SPIE 7733, Ground-Based and Airborne Telescopes III*, Vol. 77332R, pp. 1002–1012.
- [21] Cash, M., Bruch, D., Jahn, B., and Keas, P., 2008, “Practical Considerations of Joint Friction and Backlash in Large Ground-Based Telescope Secondary Optic Positioning Systems,” *Proc. SPIE 7018, Advanced Optical and Mechanical Technologies in Telescopes and Instrumentation*, Vol. 70181T, pp. 652–663.
- [22] Gomes, R. F. P., Nijssen, J. P. A., and van Ostayen, R. A. J., 2020, “Design of a Compliant Hinge Based on Closed Form Pressure Balancing,” *Proceedings of the ASME 2020 International Design Engineering Technical Conferences and Computers and Information in Engineering Conference*, Volume 10: 44th Mechanisms and Robotics Conference (MR), Virtual, Online, Aug. 17–19, American Society of Mechanical Engineers Digital Collection, p. V010T10A003.
- [23] Bower, A. F., 2009, *Applied Mechanics of Solids*, CRC Press, Boca Raton, FL.
- [24] Venkiteswaran, V. K., and Su, H. -J., 2018, “A Versatile 3R Pseudo-Rigid-Body Model for Initially Curved and Straight Compliant Beams of Uniform Cross Section,” *ASME J. Mech. Des.*, **140**(9), p. 092305.
- [25] Martins, P. a. L. S., Jorge, R. M. N., and Ferreira, A. J. M., 2006, “A Comparative Study of Several Material Models for Prediction of Hyperelastic Properties: Application to Silicone-Rubber and Soft Tissues,” *Strain*, **42**(3), pp. 135–147.
- [26] Linß, S., Erbe, T., Theska, R., and Zentner, L., 2011, “The Influence of Asymmetric Flexure Hinges on the Axis of Rotation,” Proceedings of the 56th International Scientific Colloquium, Ilmenau University of Technology, Germany, Sept. 12–16.
- [27] Nijssen, J. P. A., 2022, “Compliant Full Film Lubricated Bearings: Concept Design & Development,” Ph.D. thesis, Delft University of Technology, Delft, Netherlands.
- [28] Vehar, C., Kota, S., and Dennis, R., 2008, “Closed-Loop Tape Springs as Fully Compliant Mechanisms: Preliminary Investigations,” *Proceedings of the ASME 2004 International Design Engineering Technical Conferences and Computers and Information in Engineering Conference*, Volume 2: 28th Biennial Mechanisms and Robotics Conference, Parts A and B, Salt Lake City, UT, Sept. 28–Oct. 2, American Society of Mechanical Engineers Digital Collection, pp. 1023–1032.
- [29] Farhadi Macheuposhti, D., Tolou, N., and Herder, J. L., 2015, “A Review on Compliant Joints and Rigid-Body Constant Velocity Universal Joints Toward the Design of Compliant Homokinetic Couplings,” *ASME J. Mech. Des.*, **137**(3), p. 032301.